Thermal-Piezoresistive Resonators and Self-Sustained Oscillators for Gas Recognition and Pressure Sensing

Xiaobo Guo, Yun-bo Yi, and Siavash Pourkamali, *Member, IEEE*

Abstract—This paper presents experimental and theoretical investigation of the response of microscale dual-plate thermal-piezoresistive resonators (TPRs) and self-sustained oscillators (TPOs) to different gases and pressures. It is demonstrated that the resonant frequency of such devices follow particular trends in response to the changes in the surrounding gas and its pressure. A mathematical model is derived to explain the damping dependent frequency shift characteristic of the TPO. The solution of the model indicates that the stiffness of the actuator beam decreases as the value of the damping coefficient drops at lower gas density caused by the change in the gas molecular mass or pressure. When operated in the TPR mode (linear operation), however, the frequency shift of the same silicon structure is mainly a function of gas thermal conductivity. The two different sensing mechanisms are confirmed by the measurement results showing opposite frequency shift for the TPR and TPO in helium-nitrogen mixtures. In pressure tests, frequency shifts as high as -2300 ppm are measured for a TPO by changing the air pressure from 84 to 43 kPa.

Index Terms—Thermal-piezoresistive, resonator and oscillator, thermal conductivity, damping, gas density.

I. INTRODUCTION

MICRO electromechanical systems (MEMS) have a great deal of application potentials in various sensing areas, such as gas sensing and pressure sensing. Gas sensors have a wide variety of applications in different industries as well as for environmental research and safety monitoring. For example, highly sensitive, selective, robust and cost-efficient gas sensors are required for leakage detection of explosive gases such as hydrogen and methane, and for real-time sensing of pathogenic or toxic gases. Such sensors can be divided into two categories based on their sensing mechanism: chemical and physical.

Chemical sensors are based on the chemical reaction between the target gases and the sensors. Chemical hydrogen sensors, for example, utilize palladium (Pd) [1] and platinum (Pt) [2] as catalyst to absorb hydrogen for further oxidation-reduction reactions. On the other hand, physical gas sensors operate based on specific physical properties of the target gas, such as thermal conductivity [3], [4] and density [5]. For instance, thermal conductivity gas sensors [3] and [4] have been successfully used for hydrogen sensing, as hydrogen has a much higher thermal conductivity [0.183 W/ (m·K)] compared with air [0.0263 W/ (m·K)]. Once a thermal conductivity sensor is exposed to hydrogen, the warmer part of the sensor dissipates heat to the surroundings much faster leading to a drop in its temperature, which results in reduction of the electrical resistance of the sensor. In general, physical gas sensors can be much cheaper due to their much simpler sensing mechanism and more reliable and durable over long term due to elimination of the chemical contamination/degradation problems.

In pressure sensing, MEMS technology has led to high performance and commercially viable solutions. Most of such sensors work based upon the measurement of the static deformation of a diaphragm caused by a pressure difference between the two sides. Typically, a constant pressure is fed to one side of the diaphragm using a pressure chamber while the other side encounters the variable pressure to be measured. The diaphragm deformation can be measured using different mechanisms, including optical [6], capacitive [7], piezoresistive [8] and resonant frequency shift [9], [10] methods. Among such, resonant pressure sensors have the advantages of simplifying readout system by providing an output frequency that can be directly fed into a computer (no need for A/D conversion), long term stability and higher resolution. In diaphragm-based resonant pressure sensors [9], [10], a resonant structure is attached to the diaphragm which is the preliminary sensing element. The change in the surrounding pressure deforms the diaphragm and alters the internal stress of the resonator. Consequently, the natural frequency of the resonator shifts. Alternatively, resonators [11], [12] can also be used as the primary pressure sensing element. In this approach, the change in the ambient pressure alters the damping of the resonant system and results in a resonance frequency shift. The resonant element in such pressure sensors should be in direct contact with the environment. To maximize the damping effect, such sensors take advantage of squeezed film effect by trapping a thin film of air between the resonator and the electrostatic

transduction electrodes. The excessive air damping, however, could lead to very low quality factors compromising frequency stability and measurement resolution in such devices.

High robustness and low power operation have been recently demonstrated for thermal-piezoresistive resonators (TPRs) [13]. The structural robustness and simplicity along with small size and low cost fabrication process of the TPRs make them promising candidates for various sensing applications [14], [15]. Moreover, such devices are capable of operating as fully electro-mechanical thermal-piezoresistive oscillators (TPOs) [16] without the need for a sustaining electronic amplifier. In this paper, performance and behavior of such devices operated as both TPRs and TPOs for gas and pressure sensing have been studied. The theoretical analysis for the structures is also carried out to explain and justify the difference in response behavior of TPOs and TPRs.

II. DEVICE DESCRIPTION

Fig. 1 shows the scanning electron microscope (SEM) views of a dual-plate silicon structure which can be operated in both TPR and TPO modes. The structures were fabricated using a single mask process [16] on a N-type silicon on insulator (SOI) substrate with device layer thickness of 10 μm and buried oxide layer thickness of 4 μm. Restricted by photolithography limits, structures with minimum actuator beam with of 2 μm were first fabricated. Consecutive thermal oxidation and oxide etch steps (in hydrofluoric acid) were then used to narrow down the thermal actuator beams. The submicron width of the thermal actuator beams (shown in Fig. 1), achieved by such technique, is used to reduce the required bias current and therefore the power consumption for reaching self-oscillation.

The dual-plate silicon structures shown in Fig. 1 can be operated as a regular resonator under forced actuation by applying a combination of a DC and AC currents through the structure. Due to the higher resistance of the actuator beams, most of the resulting Joule heating (electrical ohmic loss) will occur in the actuator beams that serve as both thermal actuators and piezoresistive sensing elements. The fluctuating current causes the actuator beams to expand and contract periodically. The periodic thermal stress can actuate the structure in its fundamental in-plane extensional mode, where the two plates move back and forth in opposite directions. The resulting stress from amplified mechanical vibrations at resonant frequency along with the piezoresistive effect leads to fluctuations in electrical resistance of the actuator beams. The applied DC bias current is therefore modulated by the resistance fluctuations producing an AC output current component that indicates the vibration amplitude of the resonator.

The resonant structure in Fig. 1 can also be operated as a TPO by passing a large DC current through the structure. If the DC bias is large enough, any random mechanical noise in the structure can be amplified by the following sequence leading to sustained oscillations at the mechanical natural resonant frequency of the structure. The sequence is as follows: if mechanical noise causes the plates to move slightly farther from each other, the resulting tensile stress in the actuator beams along with the negative piezoresistive coefficient of
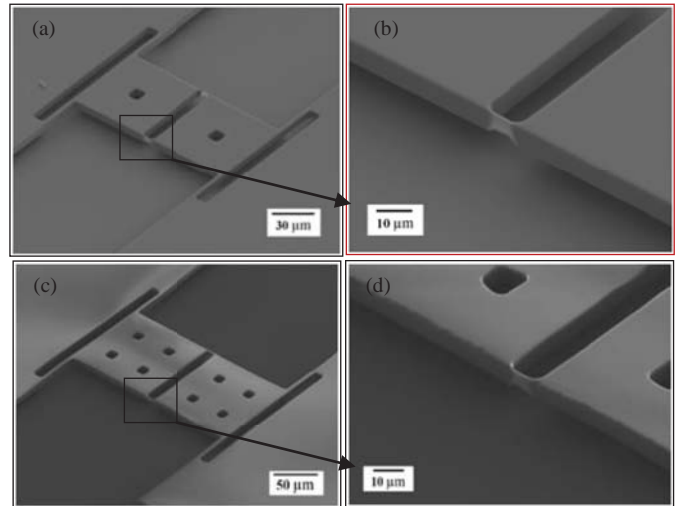

Fig. 1. The scanning electron microscope (SEM) view of two dual-plate silicon resonant structures: (a) The structure with small plates (60 μm × 60 μm) and (b) the zoomed-in view of its actuator beam. (c) The structure with large plates (99 μm × 99 μm) and (d) the zoomed-in view of its actuator beam.

N-type silicon reduces the electrical resistance of the actuator beams. Under a constant bias current, the reduced resistance is translated into lowered Joule heating which cools the actuator beams down and forces them to contract. Upon contraction, the inertia of the plates causes an over-contraction in the actuator beams. The resulting compressive stress increases the electrical resistance of the actuator beams due to the piezoresistive effect. The increase in the resistance leads to higher Joule heating and eventually re-expansion of the actuator beams. Provided that the overall energy gain in the whole cycle of the events equals the energy loss caused by the total damping of the vibrating system, self-sustained oscillation can be initiated and maintained in a stable state.

III. SENSING MECHANISM

Although both the TPO and the TPR operation modes are based on thermal actuation and can be realized by the same structure, their different operation mechanisms considerably differentiates their response to the change in the surrounding gases and the ambient pressure. The behavior of thermal-piezoresistive resonant structures under both operating configurations is analyzed in this section. Taking the symmetrical geometry of the resonant structures (shown in Fig. 1) into account, the dual-plate silicon structures can be treated as an one degree of freedom spring-mass system.

A. Thermal Conductivity Based Analysis of TPR/TPO

The temperature difference between the TPR/TPO and their surroundings is mainly maintained with Joule heating caused by the DC bias current. The generated heat is dissipated through conduction to the ambient gas and the substrate of the resonator, convection and radiation. The convection and radiation are usually negligible for the temperature range of the resonators and their small dimensions [17], [18]. When the dual plate silicon structure is heated by the DC bias,

the temperature change in the resonators can be directly related to the change in their resonance frequencies f which is

$$f = 1/2\pi \sqrt{k/m} \tag{1}$$

where m is the mass of the resonance plates and k is the stiffness of the actuator beams (spring). For most solids including silicon, the young's modulus and therefore structural stiffness k decreases as temperature increases [19]:

$$k = k_0 + c_T T_{beam} \tag{2}$$

where c_T, k_0 and T_{beam} are the temperature coefficient of the young's modulus, the actuator beam stiffness at $0K$ and the temperature of the actuator beam, respectively. When the surrounding gas changes from one gas to another gas with higher thermal conductivity, more heat will be dissipated via gas conduction from the plate into the surroundings and therefore the temperature of the TPR/TPO drops. This causes an increase in the stiffness of the actuator beams which in turn results in a higher resonance frequency.

The change in heat dissipation ΔP_{dis} through the ambient gas is [20]:

$$\Delta P_{dis} = S_{plat} A_{plat} \Delta \kappa_{gas} (T_{plat} - T_{amb}) \tag{3}$$

where S_{plat} is the shape factor, A_{plat} is the surface area of the plate, $\Delta \kappa_{gas}$ is the change in thermal conductivity of the surrounding gas, T_{plat} and T_{amb} denote the temperature of the plate and the ambient gas, respectively. Based on (3), the TPR/TPO with larger plate area A_{plat} and higher temperature T_{plat} will lead to a higher frequency shift.

B. Damping-Based Analysis of TPR

In the case of TPR operation mode (under forced linear vibration), the resonator should satisfy the following equation of motion:

$$m\ddot{x} + c\dot{x} + kx = F_{th}\cos(\omega t) \tag{4}$$

where F_{th} is the harmonic thermal force generated by the combination of a AC and DC currents, c is the damping coefficient and ω is the angular frequency of the AC input. This is a classic damped-resonance problem where the damped resonance frequency is given by:

$$f = 1/2\pi \sqrt{k(1 - 2\zeta^2)/m} \tag{5}$$

where the damping ratio ζ is defined as

$$\zeta = c/(2\sqrt{km}). \tag{6}$$

According to (5) and (6), the frequency of the TPR has a higher value when damping imposed by the surrounding gas is smaller. Generally lower gas density [21], either due to lower gas molecular mass or lower pressure results in lower damping coefficient.

C. Damping Based Analysis of TPO

The effect of damping by surrounding gas on a TPO can however be in the opposite direction compared with that of a TPR. During the mechanical vibration (oscillation) of the TPO, the fluctuation amplitude of the Joule heating ΔP in the actuator beams is given by the product of its periodic resistance fluctuation amplitude, ΔR, and the DC current I through it

$$\Delta P = I^2 \Delta R \tag{7}$$

and the output peak to peak oscillation voltage V_{p-p} monitored by an oscilloscope [16] is given by $V_{p-p} = I \Delta R$.

The temperature fluctuation amplitude, ΔT, in the actuator beams caused by the periodic change in Joule heating ΔP can be described by the following heat equation [20]:

$$\Delta \dot{T} = \Delta P/c_t - A_{sur}h\Delta T \tag{8}$$

where A_{sur} is the thermal dissipation area, h is the thermal dissipation coefficient and c_t is the thermal capacity of the actuator beams. Here, the term $A_{sur}h\Delta T$ represents not only the heat conduction from the actuator beam to the ambient gas, but also from the actuator beam to the substrate. The value of the thermal capacity c_t is calculated using $c_t = \rho c_p V$, where ρ, c_p and V are the density, the specific heat capacity of silicon and the total volume of the actuator beams, respectively.

By adding the periodic change in the length of the actuator beams, x, driven by the periodic change in its temperature ΔT, the equation of motion for the spring-mass-damper system turns into:

$$m\ddot{x} + c\dot{x} + k(x - \alpha l \Delta T) = 0 \tag{9}$$

where α is the thermal expansion coefficient of silicon and l is the initial length of the actuator beams. The stiffness of the actuator beams is calculated by $k = EA_{sec}/l$, where E is the young's modulus of silicon and A_{sec} is the total cross-sectional area of the actuator beams.

The normal stress σ generated in the actuator beams is defined as:

$$\sigma = k(x - \alpha l \Delta T)/A_{sec}. \tag{10}$$

The change in the resistance ΔR of the actuator beams due to the piezoresistive effect is:

$$\Delta R = \pi_l \sigma R_0 \tag{11}$$

where π_l is the piezoresistive coefficient and R_0 is the resistance of the actuator beams under no stress.

Substituting (7), (10) and (11) into (8), results in:

$$\Delta \dot{T} = Nk(x - \alpha l \Delta T) - A_{sur}h\Delta T \tag{12}$$

where N is defined as $N = I^2 \pi_l R_0/(c_t A_{sec})$.

Substituting (12) into (9), results in:

$$\Delta \dddot{T} + (Nk\alpha l + A_{sur}h + c/m)\Delta \ddot{T} + (cNk\alpha l + cA_{sur}h + k)\Delta \dot{T}/m + kA_{sur}h\Delta T/m = 0. \tag{13}$$

Under periodic dynamic conditions, the temperature change ΔT has the form $\Delta T = \Delta T_0 e^{i\omega t}$. Substituting the

temperature change ΔT in the phasor form into (13), leads to:

$$-i\omega^3 - (Nk\alpha l + A_{sur}h + c/m)\omega^2 + (cNk\alpha l$$
$$+cA_{sur}h + k)i\omega/m + kA_{sur}h/m = 0. \quad (14)$$

For (14) to be satisfied, both the real and imaginary parts should each be equal to zero which results in

$$(Nk\alpha l + A_{sur}h + c/m)\omega^2 = kA_{sur}h/m \quad (15)$$

and

$$\omega = \sqrt{(cNk\alpha l + cA_{sur}h + k)/m}. \quad (16)$$

Substituting (16) into (15), the following equation is obtained:

$$(mNk\alpha l + mA_{sur}h + c) \times (cNk\alpha l + cA_{sur}h + k)$$
$$= mkA_{sur}h \quad (17)$$

where

$$c = -(k \pm \sqrt{S})/(2(A_{sur}h + Nk\alpha l))$$
$$- (mA_{sur}h + mNk\alpha l)/2 \quad (18)$$

and

$$S = A_{sur}^4 h^4 m^2 + 4A_{sur}^3 h^3 m^2 Nk\alpha l + 6A_{sur}^2 h^2 m^2 N^2 k^2 \alpha^2 l^2$$
$$+ 2A_{sur}^2 h^2 km + 4A_{sur}hm^2 N^3 k^3 \alpha^3 l^3 + m^2 N^4 k^4 \alpha^4 l^4$$
$$+ 2mN^2 k^3 \alpha^2 l^2 + k^2. \quad (19)$$

However, the power dissipation caused by the term $A_{sur}h\Delta T$ in (8) is negligible compared to the total input electrical power [13]. Neglecting the term $A_{sur}h\Delta T$ simplifies (17) to:

$$(mNk\alpha l + c)(cNk\alpha l + k) = 0 \quad (20)$$

which results in:

$$c = -mNk\alpha l. \quad (21)$$

In (21), the energy loss caused by the damping effect is represented by the damping coefficient c, while the energy gain from the thermal-piezoresistive-mechanical coupling is indicated by the term $-mNk\alpha l$. To initiate and maintain oscillation, it is important to generate enough energy to counteract the energy loss. Since the damping coefficient c is positive, the device should necessarily have a negative piezoresistive coefficient (N-type single crystal silicon). Assuming the fixed geometry of a TPO, there has to be a minimum input current (or DC power $I^2 R_0$) through the TPO to meet (21) for initiating and maintaining its oscillation.

If the energy loss is higher than the energy gain, the oscillation will vanish, while the vibration energy will keep increasing if the energy gain is higher than the energy loss. The increased vibration energy comes from the excessive energy gain after the losses of energy are compensated in every cycle. The amplitude increase will be accumulated in successive cycles, and theoretically, in a completely linear system, the vibration energy will keep increasing until a mechanical failure happens in the system. However, in reality, the stiffness of the actuator beams shows significant nonlinearity [22]. The nonlinear stiffness term reduces the overall stiffness as the vibration amplitude increases.

The changes in the density of gas, such as the change in the gas molecular mass or pressure, disrupts the balance between the two sides of (21) by altering the damping coefficient. If the energy loss is reduced because of the lower damping under lower gas molecular mass or lower gas pressure, the energy gain in each oscillation cycle becomes higher than the energy loss. Therefore, the vibration amplitude starts to increase until the actuator beams' mechanical nonlinearity decreases the stiffness of the actuator beams k, eventually putting the oscillation in another stable state as (21) is satisfied.

Based on (21), the changes in the stiffness of the actuator beams dk is:

$$dk = -dc/(mN\alpha l) \quad (22)$$

where dc is the change in damping coefficient. Equation (22) shows that for smaller values of input currents (or DC power) and therefore smaller value of N, larger changes in stiffness dk will occur for the same amount of the change in the damping dc for the same TPO.

On the other side, (16) can be simplified to:

$$\omega^2 = (cN\alpha l + 1)k/m. \quad (23)$$

Since $cN\alpha l \ll 1$, (23) can be further simplified to

$$\omega^2 \approx k/m. \quad (24)$$

Equation (24) indicates a lower stiffness for the actuator beams, results in a lower oscillation frequency. As it was discussed for (21), it could be inferred that the TPO will have a lower oscillation frequency when the damping is decreased by a drop in the density of the surrounding gas and vice versa.

IV. MEASUREMENTS

In order to perform gas and pressure sensing tests using the TPRs and TPOs, the measurements are conducted in two parts. Due to the hazards associated with handling and working with hydrogen, helium that has somewhat similar physical properties (e.g. thermal conductivity and density) was used in the experiments. Nitrogen was used to dilute helium to different concentrations because the physical properties of nitrogen are close to those of air. The TPOs and TPRs are then operated in different concentration of the helium. Whereas for pressure sensing, the TPRs and TPOs are run under both low pressures of air (in a vacuum setup) and high pressures of nitrogen (in a pressure chamber).

A. Gas Sensing Behavior of TPR/TPO

Fig. 2 shows (a) the camera picture and (b) the schematic diagram of the experiment setup used to characterize the sensory behavior of the TPRs/TPOs. The pressure in the gas chamber was kept constant during the measurements. The silicon chips containing the dual-plate resonant structures were mounted on a printed circuit board (PCB) and placed in a gas chamber. For testing the devices in their TPR mode, the concentration range of helium in nitrogen was changed from zero to a 1:2 ratio. Since the structures show higher sensitivities in their TPO mode, a smaller range of the helium concentrations in nitrogen (from zero to a 1:5 mixture of
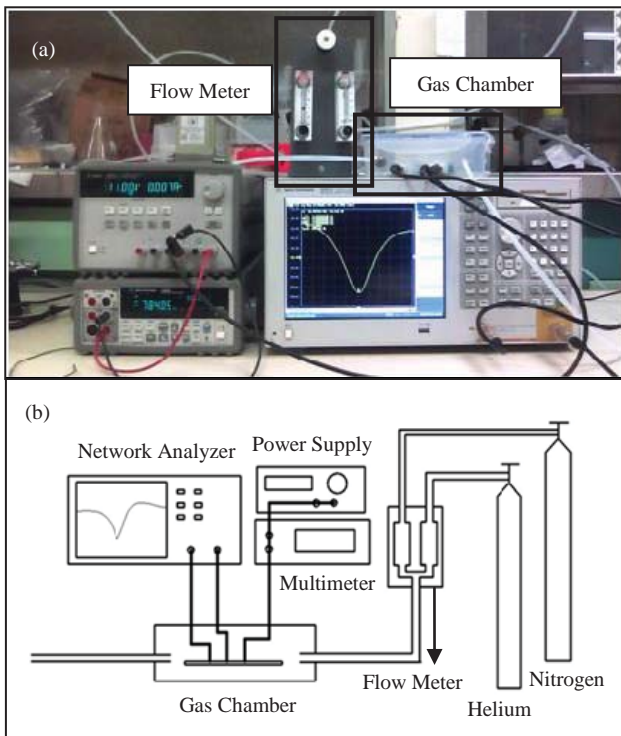
Fig. 2. (a) The camera picture and (b) the schematic diagram of the experimental setup used to characterize the frequency behavior of the MEMS devices operated as TPRs in different gas mixtures. The frequency shifts of the TPRs were measured by a network analyzer. To test the MEMS devices operated as TPOs, the network analyzer should be replaced by an oscilloscope for measuring V_{p-p} or with a frequency counter to measure the frequency. At the same time, the DC should be increased to the threshold value to excite the self-sustained oscillation.
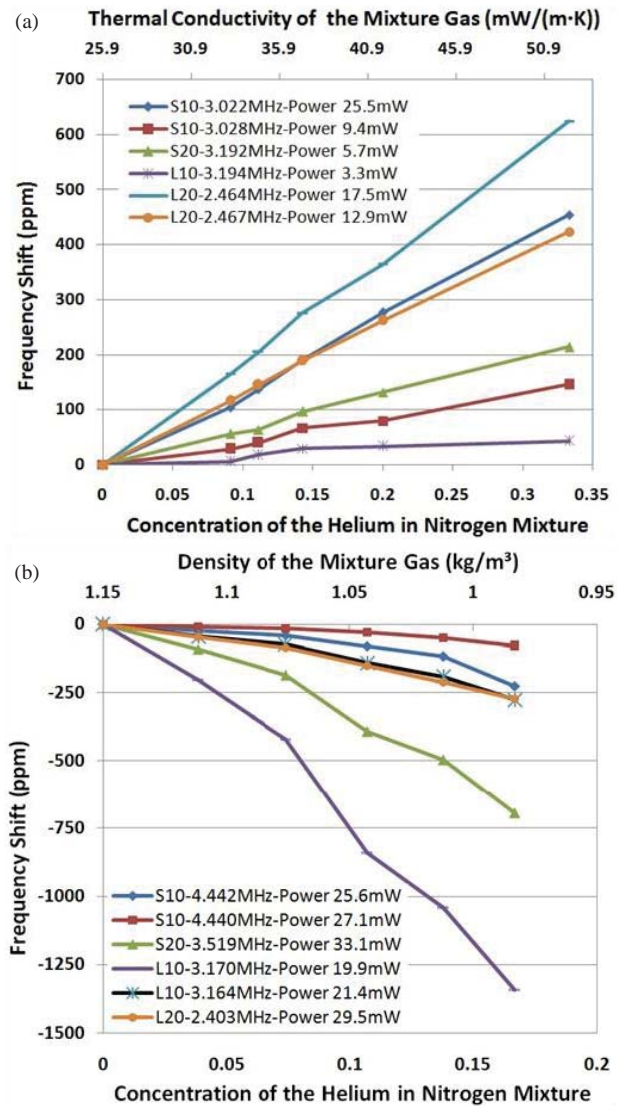

Fig. 3. Measured frequency shifts for different resonant structures in different gas mixtures, (a) working as TPRs and (b) working as self-sustained TPOs. The frequency shifts (in ppm) are with respect to their natural frequency in pure nitrogen.

helium-nitrogen) was used. Four different geometries of the MEMS devices were used in the experiments, labeled as S10, S20, L10 and L20, in which "S" and "L" stand for small plate (60 μm $\times$ 60 μm) and large plate (99 μm $\times$ 99 μm), respectively (Fig. 1). Also, "10" and "20" stand for the actuator beam lengths which are 10 μm and 20 μm, respectively. Measurements were performed under different input DC powers.

The DC power consumption and corresponding frequencies measured for different dual-plate silicon structures in nitrogen are shown in the legend of Fig. 3. Fig. 3(a) shows the measured frequency shifts for different TPRs under different helium concentrations in nitrogen. As expected, the resonance frequency of all TPRs increase as the gas thermal conductivity increases (higher helium percentage). The change in the resonance frequency is almost proportional to the helium concentration. The observed maximum frequency shifts are 624 ppm in a 1:2 mixture of helium-nitrogen compared with pure nitrogen. The minimum detectable limit of the helium concentration that can be measured by this particular TPR is 0.022% (220 ppm) assuming that the minimum detectable frequency shift is 1 Hz. Comparing the frequency shifts for the same device at different DC power levels reveals that when biased at a higher DC power, the resonators show higher sensitivity. Moreover, the frequency shifts of the device with larger plate, even at lower power level (L20-17.5 mW) are higher than that of the smaller device biased at higher DC

power (S10-25.5 mW). Such conclusions confirm the results derived from the theoretical analysis. More sensitive TPRs could be realized by using the device can withstand higher input power and have larger plates.

Fig. 3(b) illustrates the measured frequency shifts for the same resonant structures working as self-sustained TPOs. As expected, such devices show an opposite trend (negative frequency shifts in higher helium concentration) compared with when they were operated as TPRs. The increased helium concentration lowers the gas mixture density leading to a reduced ambient damping and therefore a lower oscillation frequency. The experimental results are in agreement with the discussions in the previous section. Frequency shifts as high as -1340 ppm were obtained in a 1:5 mixture of helium-nitrogen with respect to pure nitrogen which shows much higher sensitivity in the TPO mode than the TPR mode. The minimum detectable limit of the helium concentration for this
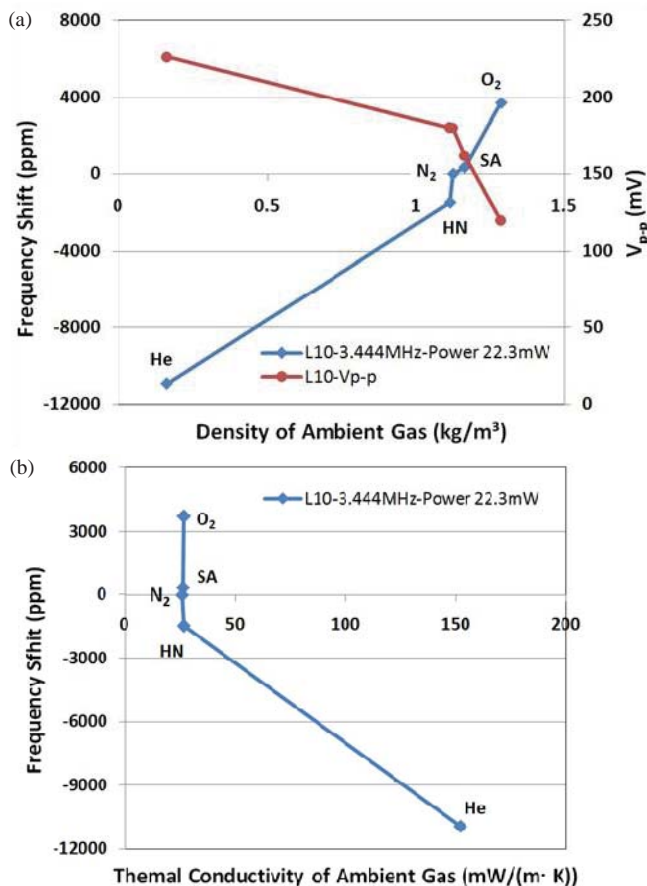
Fig. 4. A self-sustained TPO working in different gases, (a) the frequency shifts (with respect to the frequency in nitrogen) and V_{p-p} versus gas density, (b) frequency shifts versus the thermal conductivity of different gases. A strong correlation is clearly seen in (a), but there is no obvious correlation between thermal conductivity and frequency shifts.
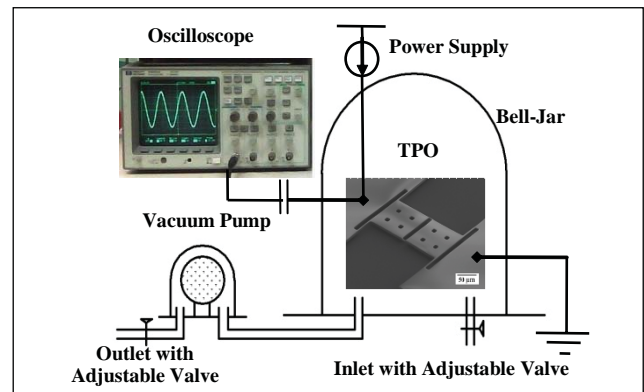

Fig. 5. The experimental setup used to characterize the frequency behavior of the TPO in different air pressure. The V_{p-p} of the TPO was measured by the oscilloscope. The frequency was monitored using a frequency counter to replace the oscilloscope. To test the frequency of the device when it was operated as TPR, the outside electrical connection should be changed as the instruction in Fig. 2b.

gas with higher density (larger molecular mass). Moreover, Fig. 4(b) shows that the frequency of the oscillator is not a function of the thermal conductivity of the surrounding gases.

B. Pressure Sensing Behavior of TPR/TPO

The measurements of the pressure sensing are presented in two separate sections: under and above atmospheric pressure test by two different experimental setups.

1) Lower Pressure Sensing: The test for characterizing TPR/TPO as pressure sensors were performed in a vacuum setup as shown in Fig. 5. The silicon chip containing the devices was placed on the printed circuit board (PCB) and embedded in a sealed bell-jar (glass vessel) [14]. A vacuum pump connected to the outlet in the sealed bell-jar was used to suck the air out and generate partial vacuum around the TPR/TPO. The pressure under the bell-jar was controlled by adjusting the air flow going through the inlet and outlet valves. The pressure inside the bell-jar is measured by a commercial pressure sensor and the data is transferred to a voltage signal that is read by a voltmeter. The frequency shift of the TPO measured by the frequency counter and the pressure read from the voltmeter were recorded automatically by a LabVIEW program. However, the peak to peak oscillation voltage V_{p-p} was manually measured by an oscilloscope, as well as the frequency response monitored by a network analyzer when the same silicon structure was operated as TPR.

The modal analysis result in COMSOL for the device "L10" in the test is demonstrated in Fig. 6, confirming the measured resonant frequency. The experimental results obtained from such device operated as TPR/TPO in low air pressure are shown in Fig. 7. Fig. 7(a) shows both the frequency shift and the peak to peak oscillation voltage of the TPO as a function of the surrounding air pressure. The frequency of the TPO was measured to be 3.456 MHz with a power consumption of 9.10 mW. A frequency shift of −2300 ppm was measured while changing the ambient air pressure from 84 to 43 kPa. Furthermore, as expected, the TPO had larger vibration amplitudes in lower surrounding air pressures indicated by the larger

particular TPO is 0.004% (40 ppm) assuming the minimum detectable frequency shift is 1 Hz. Furthermore, the frequency shifts for the same TPO with lower DC bias powers are higher, confirming the conclusion based on the mathematical model indicated in the previous section. Frequency shifts measured for the device with larger plates, even at higher power consumption (L20-29.5 mW) is higher than that of the device with smaller plates at lower power consumption (S10-27.1 mW) which shows the fact that oscillators with larger plates indicate better sensitivities. This is mainly due to the larger contact area between the plate and the ambient gas and then higher damping. Taking advantage of such rules, more sensitive TPOs can be designed and applied for future research and development.

Fig. 4 shows the measurement results for a self-sustained oscillator in different gases, including helium (He), 1% hydrogen in nitrogen (HN), nitrogen (N_2), synthetic air (SA) and oxygen (O_2). The frequency shifts of the TPO are clearly dependent on the gas density (higher density → higher frequency) in Fig. 4(a). This trend agrees with the measurements shown in Fig. 3(b) for different helium mixtures. The lower V_{p-p} at higher oscillation frequency indicates lower vibration amplitude resulting from increased damping caused by the
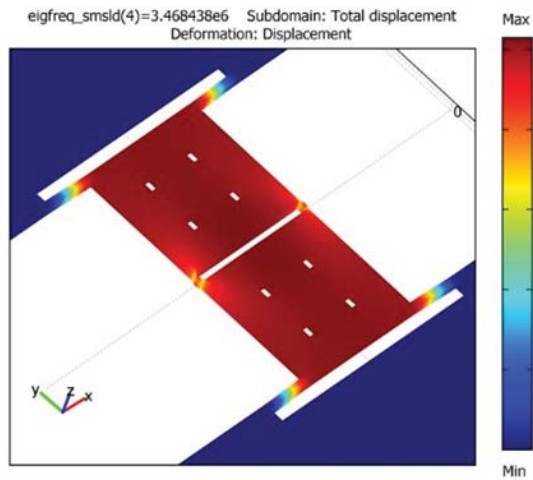
Fig. 6. The modal analysis of the device "L10." The fundamental resonance frequency is 3.468 MHz. The lower measured resonance frequency is resulted from the lower dynamic stiffness caused by the steady thermal stress and the thermally softer effect caused by the Joule heating by DC.
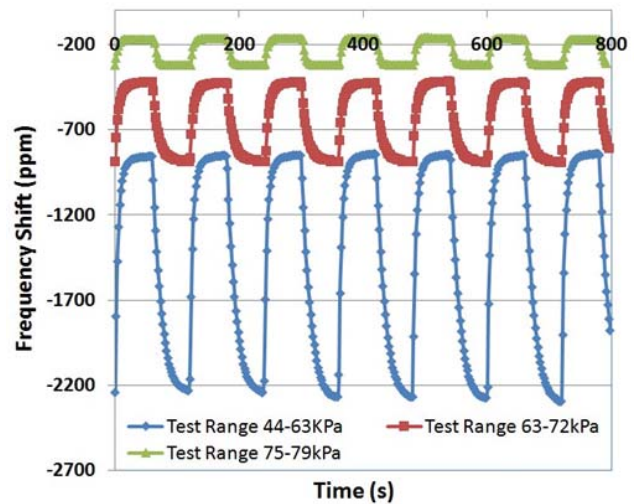

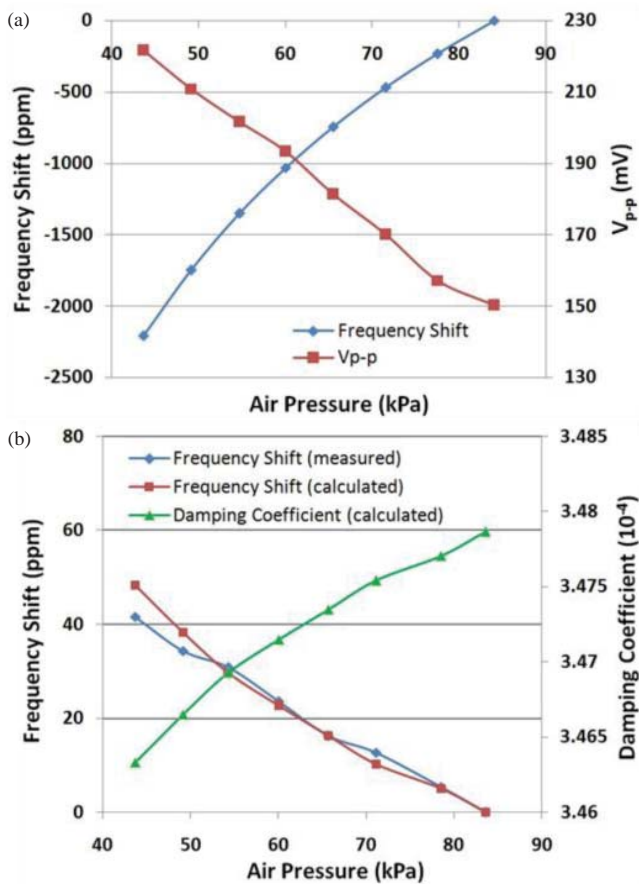Fig. 8. Frequency response of the TPO in several cycles under different air pressure ranges.

Fig. 7. (a) The experimental result of the TPO "L10" whose structure is shown in Fig. 1c. (b) The experimental result of the TPR in the same silicon structure with the calculated damping coefficient and frequency shift.

value of V_{p-p} which is proportional to the vibration amplitude. As expected from the analysis in Section III, lower damping necessitate lower stiffness to satisfy the oscillation conditions shown by (21). Due to the mechanical nonlinearity of the actuator beams, their stiffness decreases at higher amplitudes resulting in lower oscillation frequencies.

Fig. 7(b) shows the measured resonance frequency-pressure behavior of the same resonant micro-structure operated as a TPR. The resonance frequency of the TPR was measured to be 3.465 MHz with power consumption of 0.44 mW and a 0.21 mA DC. Its total frequency shift of 42 ppm was observed by changing the surrounding pressure from 84 to 43 kPa which is more than $50\times$ smaller than the absolute shift of -2300 ppm measured for the same structure in its TPO configuration. Hence, the device is much more sensitive in the TPO mode than in its TPR mode as a pressure sensor. The opposite trend in the frequency shift between the TPO and the TPR configurations is also in agreement with the conclusions made by the derivations in the previous section. Fig. 7(b) also shows the calculated damping coefficient with respect to the change in the ambient pressure. The value of the damping coefficient c was obtained based on (21) by using the measurement results of the TPO presented in Fig. 7(a), the piezoresistive coefficient of $-100 \times 10^{-12} Pa^{-1}$ [23], the measured resistance of 8160 ohm for the TPO and the thermal capacitance c_t of 1.1×10^{-12} J/K. Equation (24) was then used to calculate the stiffness k of the actuator beams (spring) of the TPO. Finally, the frequency shifts of TPRs with respect to different damping coefficients in different surrounding pressures are obtained based on (5). The calculated frequency shifts of the TPR are in good agreement with the experimental results as indicated in Fig. 7(b).

Fig. 8 shows the cyclic response of the same TPO to several cycles of pressure change in ranges of 44–63 kPa, 63–72 kPa and 75–79 kPa. The change in the pressure was controlled through a valve while all the data were collected by the LabVIEW program. When the pressure changed in a narrower range, the change in the resonant frequency of the TPO was very quick. However, there was a lag of a few seconds when the pressure change was wider, mainly because it took some time for the pressure under the bell-jar to be stabilized after the valve is closed/opened. Hence, the frequency of the TPO reacts to the changes in pressure in real time.
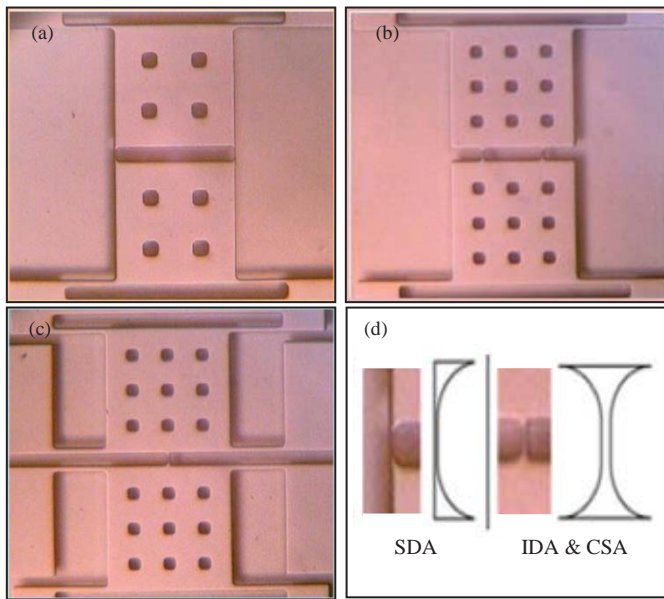
Fig. 9. The top-view of the devices with (a) the previous designed side edge dual actuator beams (SDA), (b) the new design with inner dual actuator beams (IDA) and (c) the central single actuator beam (CSA). (d) The top-view and the schematic view of the geometry of the SDA (left side), IDA and CSA (right side) actuator beams.

Fig. 10. The Result of CSA5 operated as TPO in different nitrogen pressure.

2) High Pressure Sensing: High pressure (above atmospheric pressure) measurements were performed by placing the PCB carrying the MEMS device in a sealed pressure chamber. The chamber was connected to a nitrogen gas tank. The pressure inside the chamber was increased by feeding nitrogen from the gas tank into the chamber through a pressure regulator. The pressure inside the chamber was monitored using the pressure gauge on the pressure regulator.

In the low pressure test, it was observed that some of the TPOs cannot sustain their oscillation if the ambient pressure changes significantly. One reason is that the actuator beam is too narrow to withstand higher input current which is needed to compensate the increased external damping increased in higher pressures. Another reason is due to the mechanical failure with high vibration amplitude caused by such narrow actuator beam, especially when the actuator beam becomes thermally softer under higher input currents. However, based on the conducted experiments, the device could not operate as a TPO unless the actuator beam is narrowed down to the nanoscale (as shown in Fig. 1). In practice, it is quite challenging to achieve such small sizes repeatedly and reliably. To solve this issue, an improved design was developed to achieve oscillations in broader pressure ranges. The previous device possessed side edge dual actuator beams (SDA) while the new devices employ inner dual actuator beams (IDA) and central single actuator beam (CSA) as shown in Fig. 9. The number of openings (used for releasing the structures) is reduced from four large ones to nine small ones for a better mass distribution over the plate. The device with single actuator beam can effectively decrease the power consumption. Fig. 9(d) compares the geometry of the narrowed actuator beams in SDA, IDA and CSA. Interestingly, the new devices are capable of operating as self-sustained TPOs with even
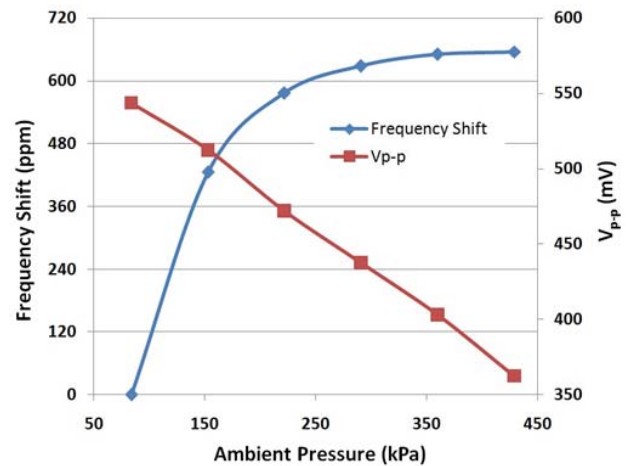
wider actuator beams. The wider and symmetrical actuator beams guarantee the TPO to work in a broader pressure range for two reasons. First, wider actuator beams can withstand higher input current to compensate more damping in higher pressure ranges. Second, the symmetrical geometry and larger width of the actuator beams result to larger stiffness of the actuator beams. Therefore, there will be a smaller vibration amplitude and hence less tensile strain to reduce the risk of mechanical failure when a higher vibration energy is provided by higher input current.

The high pressure tests were started from the atmospheric pressure and the frequency shift was recorded until oscillation was stopped as a result of the increased damping. The input current of the TPO was kept at a high level in the beginning to enlarge the pressure range under which oscillations can be sustained. Fig. 10 shows the measurement obtained from CSA5 operated as TPO in the high pressure test. The suffix number "5" after the device name represents the length of the actuator beam. The pressure range under which the CSA5/TPO could maintain self-sustained oscillations was from 84 to 429 kPa. The total frequency shift over such pressure range was measured to be 656 ppm that is two times higher than its TPR mode (-315 ppm). However, as indicated in Fig. 10, the frequency shift of the TPO shows a higher change rate at first but saturates toward the end. The input power of the TPO and the peak to peak output voltage V_{p-p} were measured to be as high as 18.69 mW and 546 mV, respectively, which are much higher than those in the low pressure test. Similar to the low pressure test, the change in the V_{p-p} shows a linear relationship as the pressure changes indicated in Fig. 10.

All other measurements obtained from the TPOs operated in the high pressure test are briefly listed in Table I. As expected, all the TPOs showed higher frequencies as the ambient pressure was increased. In the group of IDA/TPOs, the workable pressure range of IDA15 was higher than IDA5 for its higher input power. In addition, IDA15 also showed the maximum sensitivity among all the TPOs. In the group of CSA/TPOs, CSA5 had the broadest workable pressure range and its working power was also the highest among the CSA/TPOs. In conclusion, the workable pressure ranges of

TABLE I
HIGH PRESSURE MEASUREMENT OF IDAS AND CSAS

Device	I (mA)	P (mW)	f (MHz)	ΔPr (kPa)	Δf (ppm)
IDA5	1.41	5.93	8.233	<7	–
IDA15	4.87	35.52	5.677	138	1671
CSA3	4.08	13.47	6.284	28	18
CSA5	3.88	18.69	5.376	345	656
CSA10	3.24	14.58	4.867	179	50

I is the input current, P is the input power f is the frequency at atmospheric pressure (84 kPa in Denver); ΔPr is the workable pressure range and Δf is the frequency shift in such pressure range.

IDA/TPOs or CSA/TPOs are broader if they can withstand a higher input electrical power.

V. CONCLUSION

Gas recognition and pressure sensing capability of MEMS resonant structures operating as both TPRs/TPOs were investigated. The theoretical analysis and the experimental measurements show that TPRs are more sensitive to the thermal conductivity of the surrounding gas while the frequency shift of the TPOs is mainly affected by the damping resulting from the surrounding gas (a function of gas species and pressure). The sensitivity trends of the TPOs and the TPRs derived from mathematic models were also confirmed by the measurements.

A much higher frequency shift were observed in the experiments for the TPOs compared with the TPRs resulting from the same change in the helium concentration. The response of the TPOs to the changes in gas pressure were also measured to be $50\times$ larger than that of the same micro structure when it was operated as a TPR. New TPO designs that are more suitable for operation under higher pressure range were also successfully realized and tested.

In addition to the higher sensitivity of the TPOs than the TPRs showed by the measurement, devices operating in their TPOs mode also have a simpler working mechanism as their vibration is only driven by a DC current. The TPRs/TPOs with robust monolithic crystalline silicon structures can be exposed to the environment directly. Batch-fabrication of such devices using simple and well-established MEMS fabrication techniques can decrease the cost significantly. The TPRs can be applied as low cost thermal conductivity gas sensors, while the TPOs have more potential as low cost gas density sensors or pressure sensors.

REFERENCES

[1] S. Sekimoto, H. Nakagawa, S. Okazaki, K. Fukuda, S. Asakura, T. Shigemori, and S. Takahashi, "A fiber-optic evanescent-wave hydrogen gas sensor using palladium-supported tungsten oxide," *Sens. Actuators B, Chem.*, vol. 66, nos. 1–3, pp. 142–145, 2000.

[2] K. Tsukada, T. Kiwa, T. Yamaguchi, S. Migitaka, Y. Goto, and K. Yokosawa, "A study of fast response characteristics for hydrogen sensing with platinum FET sensor," *Sens. Actuators B, Chem.*, vol. 114, no. 1, pp. 158–163, 2006.

[3] I. Simon and M. Arndt, "Thermal and gas-sensing properties of a micro machined thermal conductivity sensor for the detection of hydrogen in automotive applications," *Sens. Actuators A, Phys.*, vols. 97–98, pp. 104–108, Apr. 2002.

[4] P. Tardy, J. Coulon, C. Lucat, and F. Meniland, "Dynamic thermal conductivity sensor for gas detection," *Sens. Actuators B, Chem.*, vol. 98, no. 1, pp. 63–68, 2004.

[5] D. Zeisel, H. Menzi, and L. Ullrich, "A precise and robust quartz sensor based on tuning fork technology for (SF6)-gas density control," *Sens. Actuators A, Phys.*, vol. 80, no. 3, pp. 233–236, 2000.

[6] S. Sekimoto, H. Nakagawa, S. Okazaki, K. Fukuda, S. Asakura, T. Shigemori, and S. Takahashi, "Miniature all-silica optical fiber pressure sensor with an ultra thin uniform diaphragm," *Opt. Exp.*, vol. 18, no. 9, pp. 9006–9014, 2010.

[7] E. Bakhoum, "Capacitive pressure sensor with very large dynamic range," *IEEE Trans. Compon. Packag. Technol.*, vol. 33, no. 1, pp. 79–83, Mar. 2010.

[8] X. Li, Q. Liu, S. Pang, K. Xu, H. Tang, and C. Sun, "High-temperature piezoresistive pressure sensor based on implantation of oxygen into silicon wafer," *Sens. Actuators A, Phys.*, vol. 179, pp. 277–282, Jun. 2012.

[9] D. Chen, L. Liu, and Z. Wu, "A micromachined resonant pressure sensor with DETFs resonator and differential structure," in *Proc. IEEE Sensors*, Oct. 2009, pp. 1321–1324.

[10] Q. Li, S. Fan, Z. Tang, and W. Xing, "Non-linear dynamics of an electrothermally excited resonant pressure sensor," *Sens. Actuators A, Phys.*, vol. 188, pp. 19–28, Dec. 2012.

[11] M. Andrews, G. Turner, P. Harris, and I. Harris, "A resonant pressure sensor based on a squeezed film of gas," *Sens. Actuators A, Phys.*, vol. 36, no. 3, pp. 219–226, 1993.

[12] P. Schwarz, D. Feili, R. Engel, N. Pagel, and H. Seidel, "Vacuum pressure and gas detection with a silicon based micromechanical squeeze film sensor," *Proc. Eng.*, vol. 5, pp. 750–753, Sep. 2010.

[13] A. Rahafrooz and S. Pourkamali, "High frequency thermally actuated electromechanical resonators with piezoresistive readout," *IEEE Trans. Electron Devices*, vol. 58, no. 4, pp. 1205–1214, Apr. 2011.

[14] A. Hajjam, J. Wilson, and S. Pourkamali, "Individual air-borne particle mass measurement using high frequency micromechanical resonators," *IEEE Sensors J.*, vol. 11, no. 11, pp. 2883–2890, Nov. 2011.

[15] A. Hajjam and S. Pourkamali, "Fabrication and characterization of MEMS-based resonant organic gas sensors," *IEEE Sensors J.*, vol. 12, no. 6, pp. 1958–1964, Jun. 2012.

[16] A. Rahafrooz and S. Pourkamali, "Fully mircomechanical piezothermal oscillator," in *Proc. Int. Electron Devices Meeting*, Dec. 2010, pp. 158–161.

[17] Z. Guo and Z. Li, "Size effect on microscale single-phase flow and heat transfer," *Int. J. Heat Mass Transfer*, vol. 46, no. 1, pp. 149–159, 2003.

[18] X. Hu, A. Jain, and K. Goodson, "Investigation of the natural convection boundary condition in microfabricated structures," *Int. J. Thermal Sci.*, vol. 47, no. 7, pp. 820–824, 2008.

[19] C. Cho, "Characterization of Young's modulus of silicon versus temperature using a 'beam deflection' method with a four-point bending fixture," *Current Appl. Phys.*, vol. 9, no. 2, pp. 538–545, 2008.

[20] T. Bergman, A. Lavine, F. Incropera, and D. DeWitt, *Fundamentals of Heat and Mass Transfer*, 7th ed. New York, NY, USA: Wiley, 2011, chs. 4 and 9.

[21] T. Veijola and T. Marek, "Compact damping models for laterally moving microstructures with gas-rarefaction effects," *J. MEMS*, vol. 10, no. 2, pp. 263–273, 2001.

[22] V. Kaajakari, T. Mattila, A. Lipsanen, and A. Oja, "Nonlinear mechanical effects in silicon longitudinal mode beam resonators," *Sens. Actuators A, Phys.*, vol. 120, no. 1, pp. 64–70, 2004.

[23] C. Smith, "Piezoresistance effect in germanium and silicon," *Phys. Rev.*, vol. 94, no. 1, pp. 42–49, 1954.

Xiaobo Guo received the B.S. degree in aircraft design and engineering and the M.S. degree in solid mechanics from Northwestern Polytechnical University, Xi'an, China, in 2007 and 2010, respectively. He is currently pursuing the Ph.D. degree with the Department of Mechanical and Material Engineering, University of Denver, Denver, CO, USA. His current research interests are mainly related to the study of the multi-physical problem in micro electromechanical system by experimental and numerical method.

Yun-bo Yi received the B.S. degree in automotive engineering from Tsinghua University, Beijing, China, in 1994, the M.S. degree from the University of Missouri-Rolla (now Missouri University of Science and Technology, or MUST), Rolla, MO, USA, in 1997, and the Ph.D. degree in mechanical engineering from the University of Michigan, Ann Arbor, MI, USA, in 2001. He is an Associate Professor with the Department of Mechanical and Materials Engineering, University of Denver, Denver, CO, USA. His current research interests include the computation mechanics, including the thermoelastic damping in MEMS/NEMS, frictionally excited thermoelastic instability, percolation phenomena and applications.

Siavash Pourkamali received the B.S. degree in electrical engineering from the Sharif University of Technology, Tehran, Iran, in 2001, and the M.S. and Ph.D. degrees in electrical engineering from the Georgia Institute of Technology, Atlanta, GA, USA, in 2004 and 2006, respectively. From 2006 to 2012, he was an Assistant Professor with the Department of Electrical and Computer Engineering, University of Denver, Denver, CO, USA. Currently, he is an Associate Professor with the Department of Electrical Engineering, University of Texas at Dallas, Richardson, TX, USA. His current research interests include integrated silicon-based MEMS and micro systems, micromachining technologies, RF MEMS resonators/filters, and nano mechanical resonant sensors. He holds several issued patents and pending patent applications in the areas of silicon micro/nano mechanical resonators and filters and nanofabrication technologies, some of which have been licensed to major players in the semiconductor industry. He was a recipient of the 2011 NSF CAREER Award, the 2008 University of Denver Best Junior Scholar Award, and the 2006 Georgia Tech Electrical and Computer Engineering Research Excellence Award. He is also a silver medal winner in the 29th International Chemistry Olympiad (ICHO), 1997.